FISEVIER

Contents lists available at ScienceDirect

Journal of Applied Geophysics

journal homepage: www.elsevier.com/locate/jappgeo



2-D fast sweeping method for the factored Eikonal equation and its improvement on inversion accuracy



Guangnan Huang a,b,c,*, Qiuping Hu a,b, Songting Luo c, Hongxing Li a,b, Hua Zhang a,b, David C. Nobes a,b

- ^a State Key Laboratory of Nuclear Resources and Environment, East China University of Technology, Nanchang 330013, China
- ^b Department of Geophysics, East China University of Technology, Nanchang, Jiangxi, China
- ^c Department of Mathematics, Iowa State University, Ames, IA 50011, USA

ARTICLE INFO

Article history: Received 14 January 2018 Received in revised form 20 April 2019 Accepted 25 April 2019 Available online 7 May 2019

Keywords: Source singularity Factored eikonal equation Velocity inversion

ABSTRACT

Curvature of wavefront is very large near source point. However, plane wavefront assumption is adopted when calculating traveltimes by use of finite-difference scheme. Therefore, source singularity problem exists for all finite-difference based eikonal solvers. Traveltime error caused by the source singularity can spread from source to the whole computational domain, and make traveltimes inaccurate. The factored eikonal equation can deal with source singularity very well. The fast sweeping method (FSM) is chosen to solve the factored eikonal equation in this article (factored FSM). In principle, it decomposes solution of general eikonal equation into product of two factors. The first factor can be calculated analytically or numerically, while the second factor is the underlying function. Eikonal solver plays a significant role in velocity inversion. An accurate and efficient eikonal solver can improve the effect of tomogram. The factored FSM is adopted in the following velocity inversion. Three evaluation criteria are defined to test accuracy and convergence of velocity inversion. The first method is the rootmean-square (RMS) of traveltime residuals. The second method is the percentage perturbation of inverted against real velocity model. When inversion incorporating with the factored FSM, numerical examples show that: (1) RMS of traveltime residuals can converge to a smaller level, (2) percentage perturbation of inverted against initial velocity model is also smaller, (3) percentage ratio of inverted against real velocity model is also smaller,

© 2019 Elsevier B.V. All rights reserved.

1. Introduction

Seismic traveltime tomography can invert a few parameters (such as velocity of longitudinal- and shear- wave, quality factor and Poisson ratio, etc.). In Seismology, velocity of the Earth's interior can be inverted by use of seismic events continuously received from deployed stations (Aki and Lee 1976; Engdahl et al. 1998). Inverted velocity model is valuable in investigating oceanic ridges, continental plate subduction zone, volcanic channel, geological fault, rock formation and Mohos, etc. (Calvert and Fisher 2001; Lees 1992; Rawlinson and Fishwick 2012; Kennett et al. 1995). In resource exploration, high-resolution seismic profile greatly relies on an accurate velocity model. When executing statics and migration, one should often provide velocity model obtained by seismic traveltime inversion (Vesnaver et al. 2003; Bergman et al. 2004; Zhou 2006). In civil engineering prospecting, seismic traveltime tomography is also used to detect hidden danger of dam leakage, groundwater pollution and foundation of building, etc. (Zelt et al. 2006; Marti et al. 2008; Ajo-Franklin et al. 2006).

In the past a few decades, many traveltime calculation methods have been developed. However, it is difficult for ray-tracing method (such as shooting method, bending method, and sympletic ray-tracing method, etc.) to pass through shadow zone in very contrasted velocity models (Cerveny 2001: Wang 2014). Shortest path method is based on Fermat's principle and graph theory (Nakanishi and Yamaguchi 1986: Moser 1991; Fischer and Lees 1993). One can add a few secondary nodes on the edge of cells in order to improve traveltimes accuracy (Zhou and Greenhalgh 2006; Huang et al. 2014, 2017). Bai et al. (2009, 2010) made great efforts to improve numerical accuracy and computational efficiency for the shortest path method. Wavefront construction method constructs new wavefront by use of local ray-tracing method based on the current wavefront repeatedly, until traveltimes are computed for the whole computational domain (Ettrich and Gajewski 1996; Lambare et al. 1996; Vinje et al. 1993, 1999). Comparing with other traveltime computation methods, this method often costs too much computational amount (Leidenfrost et al. 1999). Vidale (1988, 1990) is one of the pioneers who use finite-difference scheme to calculate traveltimes. Since then, many finite-differences based eikonal solvers have been put forward (such as Hole and Zelt 1995; Qin et al. 1992; Van and Symes 1991; Podvin and Lecomte 1991; Kim and Cook 1999.). Fast-marching method (FMM) and fast sweeping method are

^{*} Corresponding author at: State Key Laboratory of Nuclear Resources and Environment, East China University of Technology, Nanchang 330013, China *E-mail address:* bobking2@126.com (G. Huang).

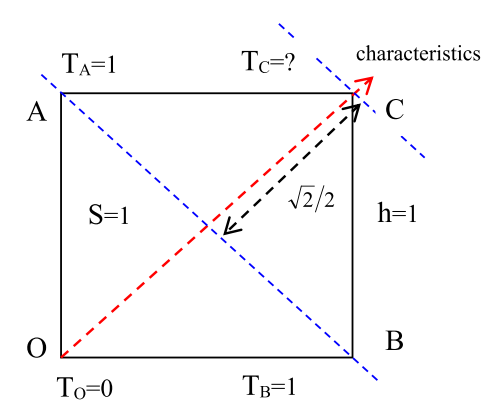


Fig. 1. A Cartesian coordinate grid configuration. In this rectangular domain, wave slowness is 1 s/km and grid spacing is 1 km. Traveltime of grid point *O* is set to 0 s. Traveltimes of point *A* and *B* are initialized along edges. Traveltime of point *C* needs to be calculated along the characteristic line.

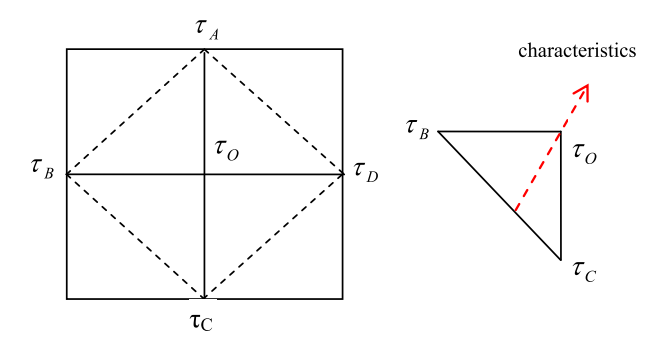


Fig. 2. Rectangular mesh. An interior grid point *O* with four neighboring points *A, B, C* and *D.*

two most promising finite-difference methods for solving the eikonal equation. Fast-marching method for the isotropic eikonal equation is put forward by Sethian and Popovici (1999). It uses narrow-band technique to describe wavefront expansion approximately when solving eikonal equation. This method is unconditionally stable and has high computational efficiency (O(NlogN), N is the total number of grid points. Fast sweeping method for the isotropic eikonal equation is an iterative method which is proposed by Tsai et al. (2003), and detailedly introduced by Zhao (2004). It uses upwind finite-difference scheme and Gauss-Seidel iterations to solve the discretized eikonal equation. This method can converge fast when given the causality condition, and it also has high computational efficiency O(N).

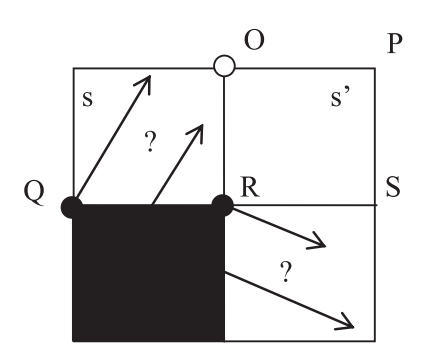


Fig. 3. Transmission wave in 2-D case. *s* and *s'* are slowness of the current and its adjacent cells

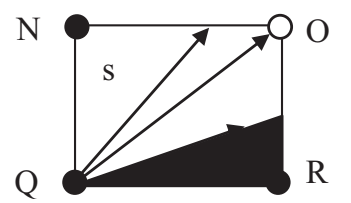


Fig. 4. Diffracted waves in 2-D case. Local shadow zone exists and corner Q acts as a secondary source.

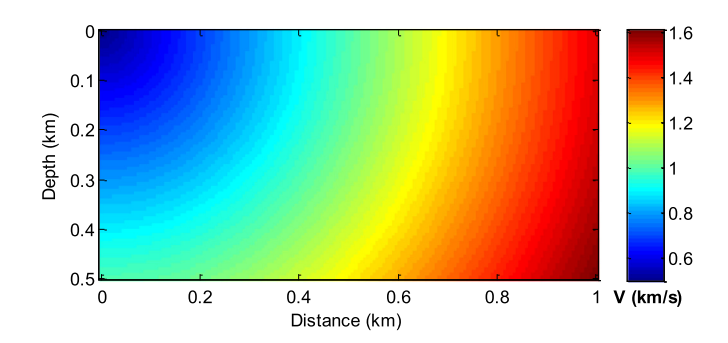
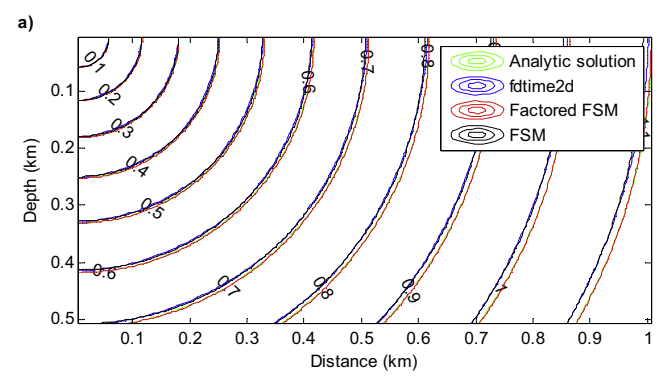


Fig. 5. 2-D constant gradient velocity model.

According to inverse theory, traveltime calculation method and inversion algorithm both play significant roles in seismic traveltime tomography. Therefore, accuracy of traveltime computation method is very important. For point source condition, source singularity problem exists for all finite-difference based eikonal solvers. Because seismic wave propagates along cell edges near source point, when one initializing traveltimes for grid points around the source. Actually, curvature of



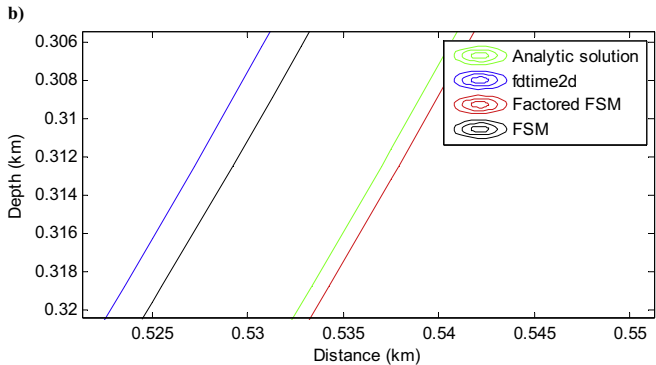


Fig. 6. Comparison of traveltime accuracy. (a) traveltimes calculated by analytical method, the FSM, the factored FSM and the Podvin method. (b) zoom-in map at 0.8 s (Green line: analytical method; red line: the factored FSM; black line: the FSM; blue line: the Podvin method).

wavefront is very large near source point, plane wavefront assumption is unreasonable. Traveltime error caused by the source singularity can make traveltimes inaccurate, even for high-order finite-difference based eikonal solver. In this study, we introduce fast sweeping method for the factored eikonal equation in order to enhance traveltime accuracy. Based on this eikonal solver, seismic traveltime tomography can improve the effect of tomogram to a certain extent.

The outline of the paper is as follows: In Section 2, traveltime error is discussed which is caused by finite-difference based eikonal solver. Large traveltime error is why we should deal with the source singularity problem. Then, we introduce fast sweeping method for the factored eikonal equation in order to deal with the source singularity. As a comparative method, another traveltime calculation method (we called it Podvin method) is recalled briefly which is proposed by Podvin and Lecomte (1991), because this method is included in the PStomo_eq velocity inversion program (Tryggvason et al. 2002). Besides, three methods to evaluate accuracy and convergence of velocity inversion are introduced. In Section 3, traveltime accuracy is compared among the analytical solution, the factored FSM, the FSM, and the Podvin method. In Section 4, the factored FSM and the Podvin method are used in PStome eq program to invert theoretical models and a field dataset, respectively. Accuracy and convergence of velocity inversion are discussed. Finally, conclusions are made for the factored FSM, and its improvement on accuracy and convergence for velocity inversion.

2. Methodology

2.1. Source singularity problem of eikonal solver

Fig. 1 is a rectangular domain with grid spacing 1 km. The wave slowness is 1 s/km in the domain. O is the source point with $T_O = 0$ s. According to finite-difference method for eikonal equation, traveltimes of grid point A and B can be calculated accurately $T_A = T_B = 1$ s. Then, we assume that seismic wave propagates along the characteristic line. Therefore, traveltime of grid point C can be calculated with plane wavefront assumption $T_C = 1 + \sqrt{2}/2$. However, the analytical solution of grid point C is $\sqrt{2}$. Percentage error of numerical traveltime against analytical solution can reach up to 20.7% for grid point C. This error always exists throughout the whole computation. It will contaminate to the whole computational domain with evolution of seismic wavefront, and makes traveltime field inaccurate.

2.2. Fast sweeping method for the factored eikonal equation

In order to deal with source singularity problem, different kinds of methods have already been put forward (Qian and Symes, 2002; Fomel et al. 2009; Luo and Qian 2012). Among which the factored FSM is one of the most effective methods. Here, we recall its principle briefly

In Seismology, first-arrival traveltime is the viscosity solution of eikonal equation (Lions 1982), and the eikonal equation can be expressed as

$$|\nabla T(\mathbf{x})|^2 = S^2(\mathbf{x}), \mathbf{x} \in \mathbb{R}^n. \tag{1}$$

It describes seismic wavefronts T(x) propagates in a slowness model S(x), in space $x \in \mathbb{R}^n$. According to the principle of factorization, solution of general eikonal equation is decomposed into a product of two factors: the first factor is solution of a simple eikonal equation, and the second factor is a necessary correction or modification. Let us consider a factored decomposition for Eq. (1)

$$S(\mathbf{x}) = S_0(\mathbf{x})\alpha(\mathbf{x}),\tag{2}$$

$$T(\mathbf{x}) = T_0(\mathbf{x})\tau(\mathbf{x}),\tag{3}$$

we assume that

$$|\nabla T_0(\boldsymbol{x})|^2 = S_0^2(\boldsymbol{x}),\tag{4}$$

where T_0 and S_0 are both canculated from analytical solution or a previous numerical computation. According to Eqs. (2)–(4), Eq. (1) can be transformed into a factorization form (Fomel et al. 2009):

$$T_0^2(\mathbf{x})|\nabla \tau(\mathbf{x})|^2 + 2T_0(\mathbf{x})\tau(\mathbf{x})\nabla T_0(\mathbf{x}) \cdot \nabla \tau(\mathbf{x}) + \left[\tau^2(\mathbf{x}) - \alpha^2(\mathbf{x})\right]S_0^2(\mathbf{x})$$
= 0, (5)

where $\alpha(\mathbf{x})$ is a constant or a slowly varying variable.

An upwind finite-difference scheme is designed in order that it can follow causality of the original eikonal equation. Numerical algorithm can be illustrated on a rectangular mesh (Fig. 2). There are four grid points (A, B, C, D) around the center point O. We can discretize Eq. (5) on these four triangles (ΔOAD , ΔOAB , ΔOBC and ΔOCD). Taking the triangle ΔOBC as an example, the discretized formulation for Eq. (5) can be written as:

$$\begin{split} T_{0}^{2}(O) \left| \left(\frac{\tau_{0} - \tau_{B}}{h}, \frac{\tau_{0} - \tau_{C}}{h} \right) \right|^{2} + 2T_{0}(O)\tau_{0}\nabla T_{0}(O) \cdot \left(\frac{\tau_{0} - \tau_{B}}{h}, \frac{\tau_{0} - \tau_{C}}{h} \right) \\ + \left[\tau_{0}^{2} - \alpha^{2}(O) \right] S_{0}^{2}(O) = 0, \end{split} \tag{6}$$

the upwind finite-difference scheme can follow causality condition when solving this equation.

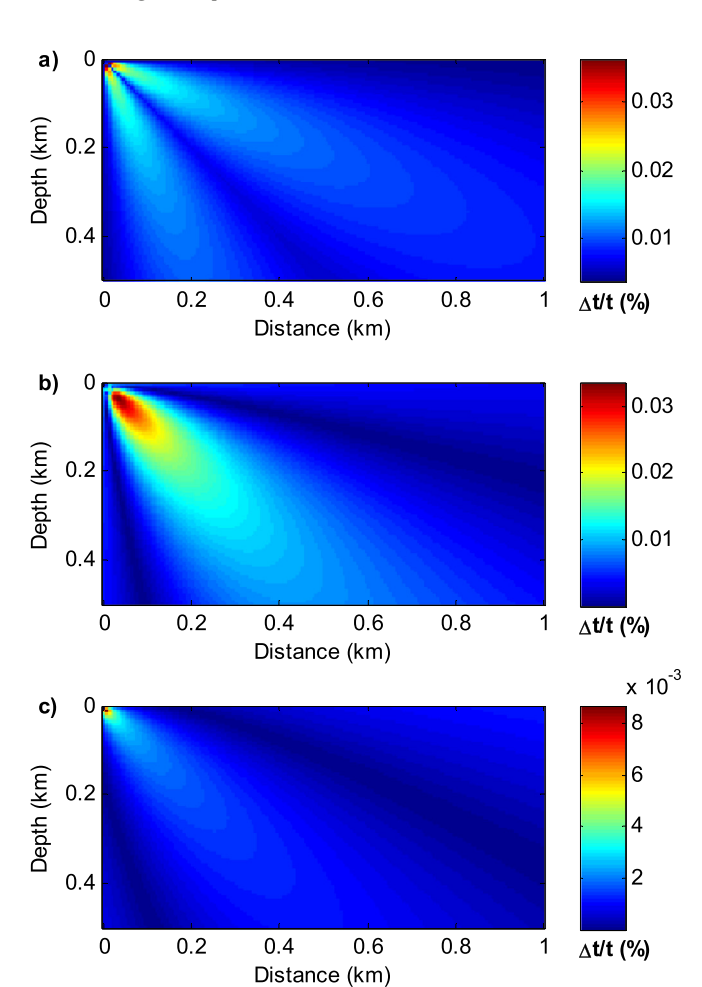


Fig. 7. Percentage error between calculated against analytical traveltimes. (a) Percentage error for the Podvin method. (b) Percentage error for the FSM. (c) Percentage error for the factored FSM.

In general, One or two real roots exist for Eq. (6). If no real root, or roots could not satisfy causality condition, the method of characteristics is adopted to pass information of τ from B to O, and from C to O.

With $(\tau_x, \tau_y) = (p, q)$, characteristic equation of Eq. (5) can be written as:

$$\begin{cases} \left(\frac{dx}{dt}, \frac{dy}{dt}\right) = \left(2T_0^2 p + 2\tau T_0 T_{0x}, 2T_0^2 q + 2\tau T_0 T_{0y}\right) = 2T_0 \nabla T \\ \frac{d\tau}{dt} = 2T_0^2 (p^2 + q^2) + 2\tau T_0 (T_{0x} p + T_{0y} q) = 2T_0 \nabla \tau \cdot \nabla T \end{cases}$$
(7)

By solving Eq. (7), two solutions (τ_{BO} and τ_{CO}) along \overrightarrow{BO} and \overrightarrow{CO} can be obtained.

Fomel et al. (2009) have already presented a local solver to calculate traveltime field for the whole computation domain. It mainly uses Gauss-Seidel iteration to sweep the computational domain with four alternating orderings repeatedly. Implementational procedures of the fast sweeping method for the factored eikonal equation are listed:

- (1) Initialization: assign initial boundary condition for boundary grid points.
- (2) Gauss-Seidel iteration: executing four sweeping orderings for the whole computational domain:
- (a) i = 1: I, j = 1: J (b) i = 1: I, j = J: 1
- (c) i = I: 1, j = 1: J (d) i = I: 1, j = J: 1
- (2.1) Discretize the factored eikonal equation on these four triangles and calculate traveltimes. For example, solve eq. (5) for two real roots $\tau_{0,\,1}$ and $\tau_{0,\,2}$ on triangle ΔOBC .
- (2.2) If two real roots $au_{0, 1}$ and $au_{0, 2}$ exist, then
- If $\tau_{O, 1}$ and $\tau_{O, 2}$ satisfy causality condition, then choose the minimal traveltime $T_{BC} = min \{\tau_{O, 1}T_{O}(O), \tau_{O, 2}T_{O}(O)\}$.
- If only $\tau_{0, 1}$ satisfies causality condition, then $T_{BC} = \tau_{0, 1} T_0(0)$.
- If only $\tau_{0, 2}$ satisfies causality condition, then $T_{BC} = \tau_{0, 2} T_0(0)$.
- (2.3) If both $\tau_{O,\,1}$ and $\tau_{O,\,2}$ can not satisfy causality condition, then calculate τ_{BO} and τ_{CO} using the method of characteristics. These two values should satisfy the causality condition $\tau_{BO}T_0(O) \ge T_B$ and $\tau_{CO}T_0(O) \ge T_G$, and choose $T_{BC} = min \{\tau_{BO}T_0(O), \tau_{CO}T_0(O)\}$.
- (2.4) Repeat (2.1)–(2.3) for T_{AD} , T_{AB} , T_{CD} in the remaining three triangles ΔOAD , ΔOAB and ΔOCD , respectively. Then, we choose the smallest one from these four traveltimes: $T_O = min \{T_{DA}, T_{AB}, T_{BC}, T_{CD}\}$.
- (2.5) Calculate $\tau_{O} = T_{O}/T_{0}(O)$.

2.3. Eikonal solver in PStomo_eq program: podvin method

The *PStomo_eq* program is an open-source seismic traveltime tomographic method which is originally developed by Harley M. Benz at the U.S. Geological Survey (Benz et al. 1996). This program was further modified by Tryggvason et al. (2009) in order to perform local earthquake tomography. It has already been used to invert velocity model and locate seismicity (Tryggvason et al. 2009; Yordkayhun et al. 2009). Traveltime computation method in the program is written by Podvin and Lecomte (1991). And the Podvin method was further modified in order to satisfy the principle of reciprocity by Tryggvason and Bergman (2006). The Podvin method is based on finite-difference approximation and Huygens principle. Transmitted waves, diffracted waves and head waves are all considered in the Podvin method. We recall its principle in this section briefly.

First arrivals generated by transmission waves. In Fig. 3, when grid point Q and R are timed only, the direction of wave propagation for point O is not entirely defined. According to the formulation of eikonal equation, two estimates for the time gradient can be computed:

$$\frac{\partial t}{\partial x} = \frac{t_R - t_Q}{h}, \frac{\partial t}{\partial y} = \pm \sqrt{s^2 - \left(\frac{t_R - t_Q}{h}\right)^2},\tag{8}$$

if the sign of $\partial t/\partial y$ is known, an estimate of arrival time at point O can be computed if it is reached by this wavefront, i.e. if $0 \le (t_R - t_O) \le hs/\sqrt{2}$.

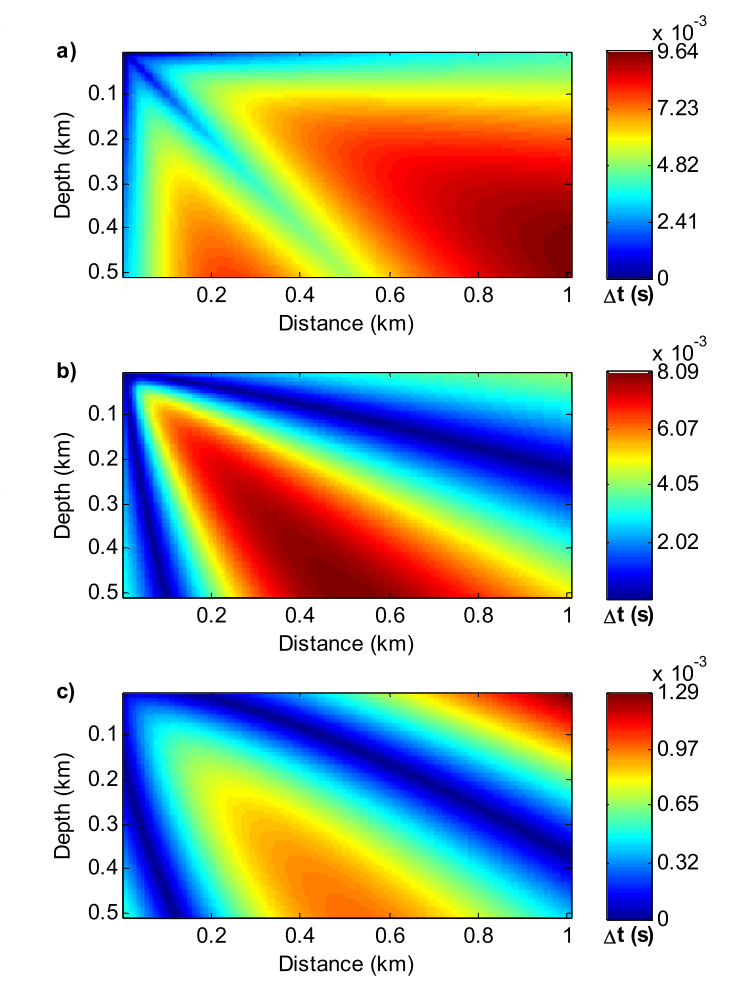


Fig. 8. Traveltime difference between calculated and analytical traveltimes. (a) traveltime difference for the Podvin method. (b) traveltime difference for the FSM. (c) traveltime difference for the factored FSM.

And if $\partial t/\partial y \ge 0$, then arrival time can be computed by:

$$t_0 = t_R + \sqrt{(hs)^2 - (t_R - t_Q)^2},$$
 (9)

In 2-D case, eight different traveltime estimates for the current point need be computed.

First arrivals generated by head waves. For transmission waves, one need to use slowness s in the current cell to compute traveltime. If slowness s of the current cell is larger than slowness s' of its adjacent cell, then a head wave should travel along edge RO. Arrival time for grid point O can be computed by $t_O = t_R + hs'$. In fact, a smaller slowness should always be chosen to calculate arrival time. Therefore, estimate of arrival time caused by head waves can be calculated with:

$$t_0 = t_R + hmin(s, s'). \tag{10}$$

In 2-D case, four different estimates of arrival time need be computed for the current point.

First arrivals generated by diffracted waves. Estimates of arrival time for grid point *O* are not realiable if a local shadow zone exists in the current cell (Fig. 4). Then, the point *Q* can be considered as a secondary source, and it emits diffracted waves propagating through point *O*. In

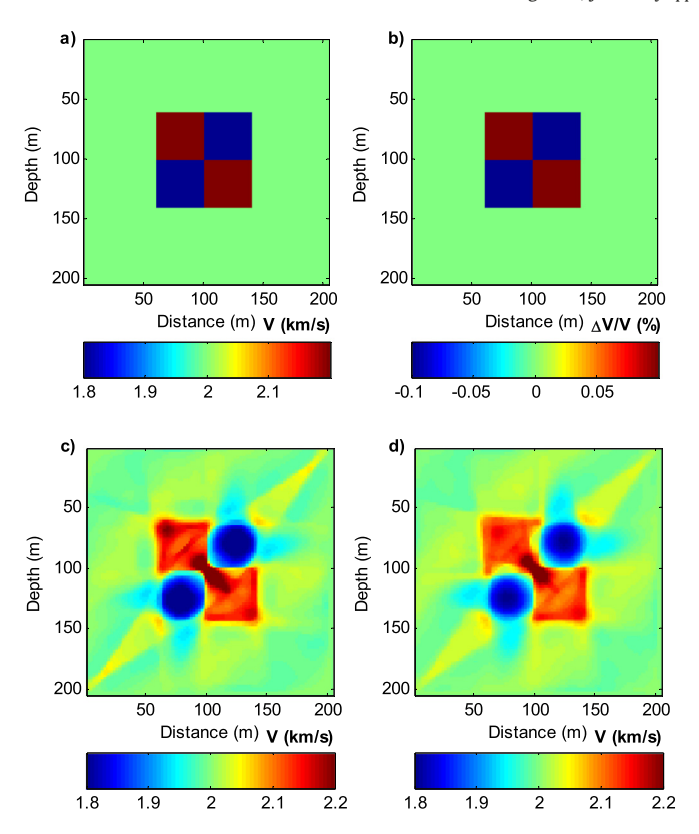


Fig. 9. Comparison of inversion results. (a) velocity model with four block anomalies. (b) the percentage perturbation of real model against the initial model. (c) velocity model obtained by the Method II. (d) velocity model obtained by the Method I.

such an occasion, arrival time for point O can be calculated as:

$$t_0 = t_0 + hs\sqrt{2}. (11)$$

In 2-D data structure, four estimates of arrival time need be computed for the current point.

2.4. Accuracy and convergence property of velocity inversion

Actually, it is impossible for inverted model to be the same as real model, regardless of theoretical or real model. Comparing with real model, inverted model can be only recovered to a certain extent. It is meaningful to estimate accuracy and convergence properties for velocity inversion. Some methods have already been proposed to evaluate

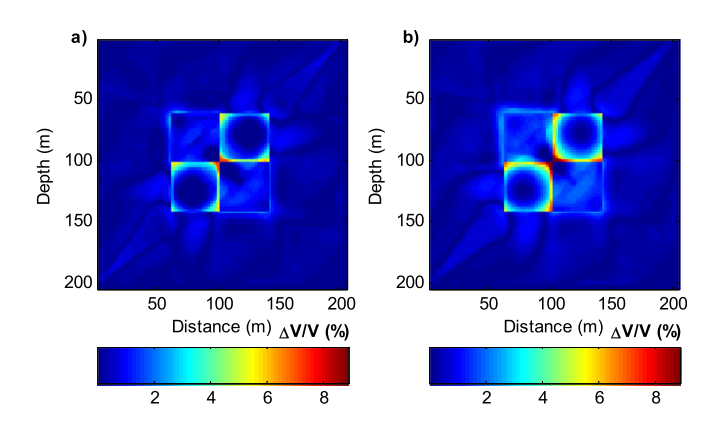


Fig. 10. Percentage perturbation of inverted against the input velocity model. (a) percentage perturbation for the Method II, (b) percentage perturbation for the Method I.

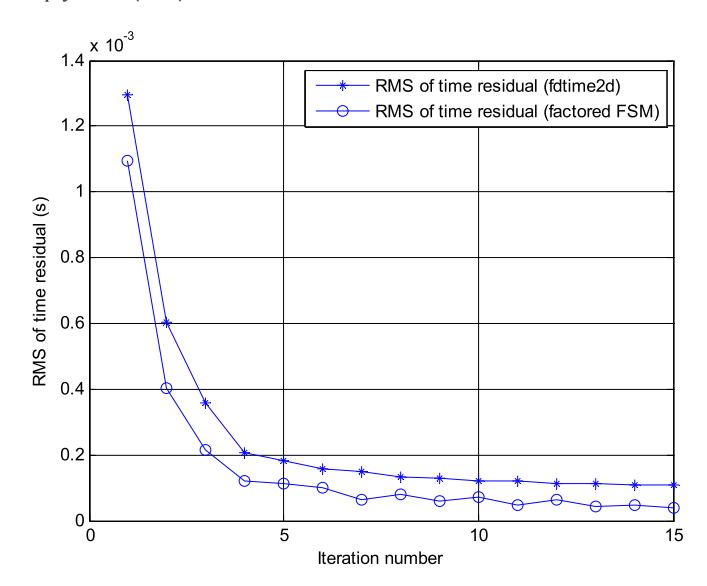


Fig. 11. Curve of RMS of traveltime residuals. (a) line with circle: convergence curve of the Method II. (b) line with asterisk: convergence curve of the Method I.

the capability for velocity inversion so far (Bai and Greenhalgh 2005; Bai et al. 2017). In order to test the superiority of the factored FSM in velocity inversion, three different kinds of evaluation criteria are listed:

Convergence level of the Traveltime Residual.

When updated model approaches to real model gradually, synthetic traveltimes can fit observed traveltimes better. Root-mean square (RMS) of traveltime residuals is defined as:

$$RMS(\delta T) = \sqrt{\frac{\sum_{i=1}^{M} \left(t_{obs}^{i} - t_{syn}^{i}\right)^{2}}{M}}.$$
(12)

where t_{obs} is observed traveltime, and t_{syn} is synthetic traveltime. M is the total number of source-receiver pairs.

Percentage Perturbation of Real against the Initial Model.

When an input velocity model is given, anomalies of velocity model can be recovered to a certain extent both in numerical value and shape. Recovery ratio of velocity model is a very important appraising index. Percentage perturbation of real against the initial model can be defined

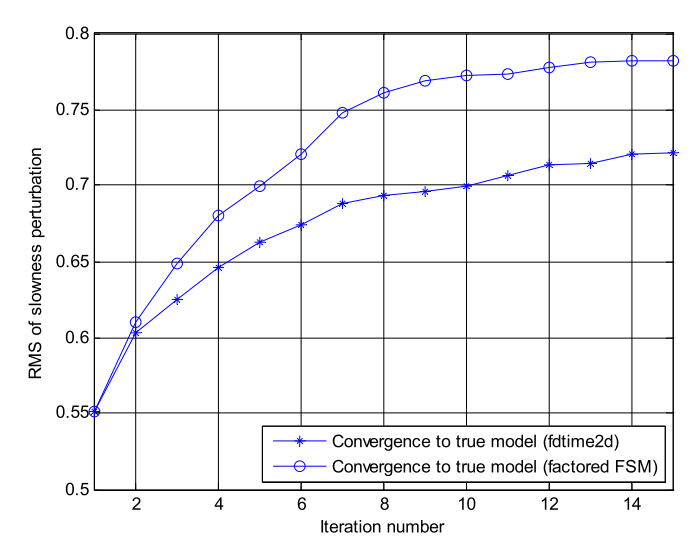


Fig. 12. Curve of percentage ratio of inverted against the real model. (a) line with circle: curve of percentage ratio for the Method II. (b) line with asterisk: curve of percentage ratio for the Method I.

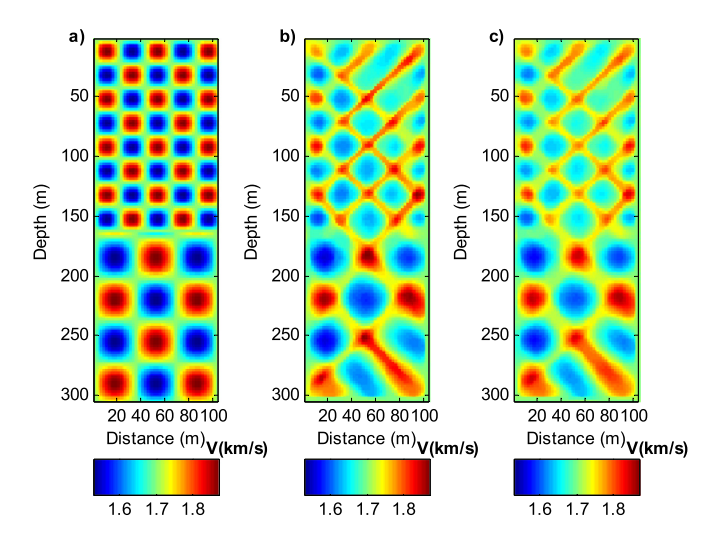


Fig. 13. Comparison of inverted velocity models. (a) the real checkerboard velocity model. (b) velocity model obtained by the Method II. (c) velocity model obtained by the Method I.

as:

$$V_{ratio} = \sqrt{\frac{\sum_{i=1}^{N} \left(\frac{V_{syn}^{i} - V_{input}^{i}}{V_{true}^{i} - V_{input}^{i}}\right)^{2}}{N}},$$
(13)

where V_{input} , V_{syn} , V_{true} are input velocity model, updated velocity model and true velocity model, respectively. N is total number of unknowns in the velocity model.

Percentage Ratio of Inverted against the Real Model.

In theory, if RMS of traveltime residuals equals to zero in velocity inversion, then inverted velocity model should be the same as real velocity model. Actually, RMS of traveltime residuals can not be zero, because multiple solutions always exist for velocity inversion in theory. Therefore, inverted model always can not be the same as real model. Percentage ratio of inverted against the real velocity model can be defined as:

$$V_{diff} = \frac{V_{sym} - V_{true}}{V_{true}} \times 100\%. \tag{14}$$

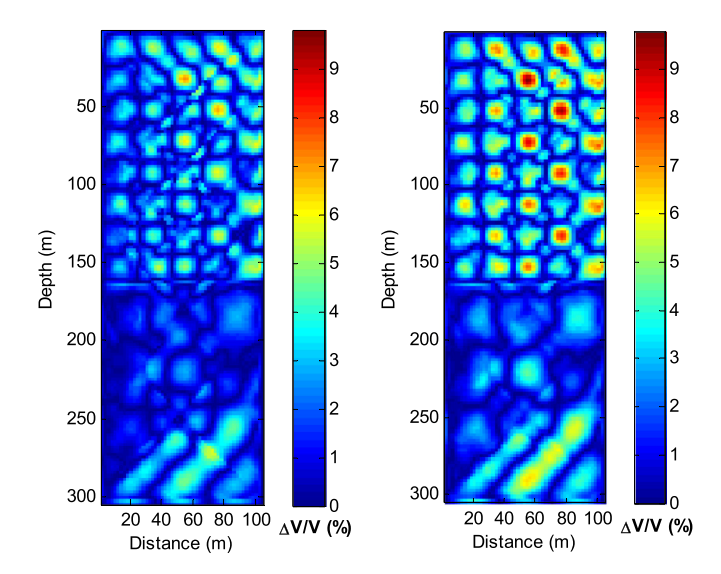


Fig. 14. Percentage perturbation of inverted against the input velocity model. (a) percentage perturbation for the Method II. (b) percentage perturbation for the Method I.

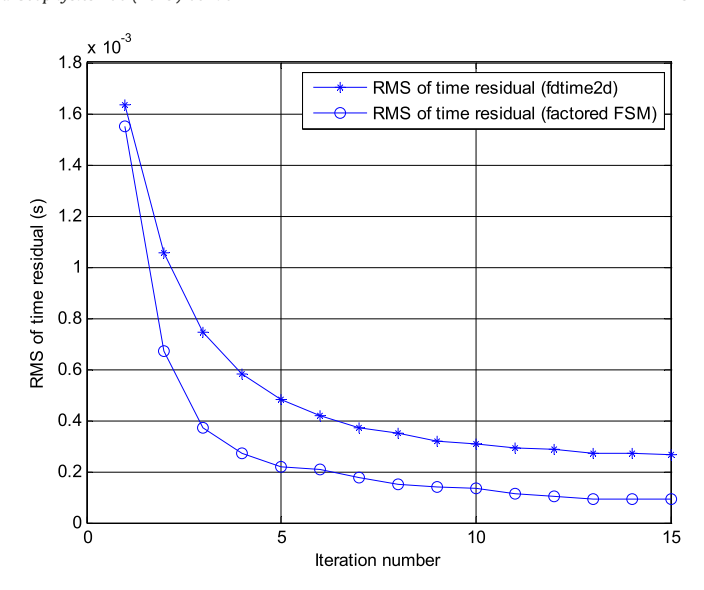


Fig. 15. Curve of RMS of traveltime residuals. (a) line with circle: convergence curve of the Method II. (b) line with asterisk: convergence curve of the Method I.

This index shows to what an extent the velocity model can be recovered.

3. Traveltime accuracy test

In order to domenstrate traveltime accuracy for the factored FSM, a constant gradient velocity model is chosen as a test model (Fig. 5). The FSM and the Podvin method are chosen as comparative methods. Analytical solution for the constant gradient velocity model is provided as a reference for the three methods.

For the velocity model, if one knows the exact location $\mathbf{x_0}$ of source point, then the slowness function can be expressed as (Fomel et al. 2009):

$$\frac{1}{S(\mathbf{x})} = \frac{1}{S_0} + \mathbf{G_0} \cdot (\mathbf{x} - \mathbf{x_0}),\tag{15}$$

where S_0 is a constant value, and G_0 is constant gradient of velocity.

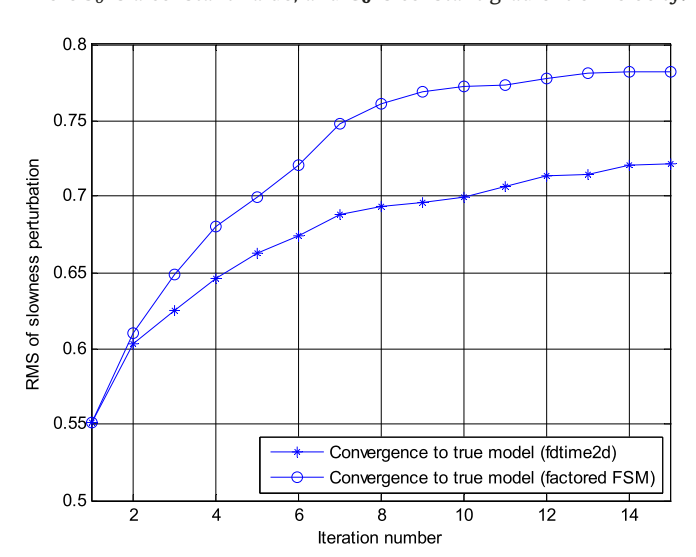


Fig. 16. Curve of percentage ratio of inverted against the real model. (a) line with circle: curve of percentage ratio for the Method II. (b) line with asterisk: curve of percentage ratio for the Method I.

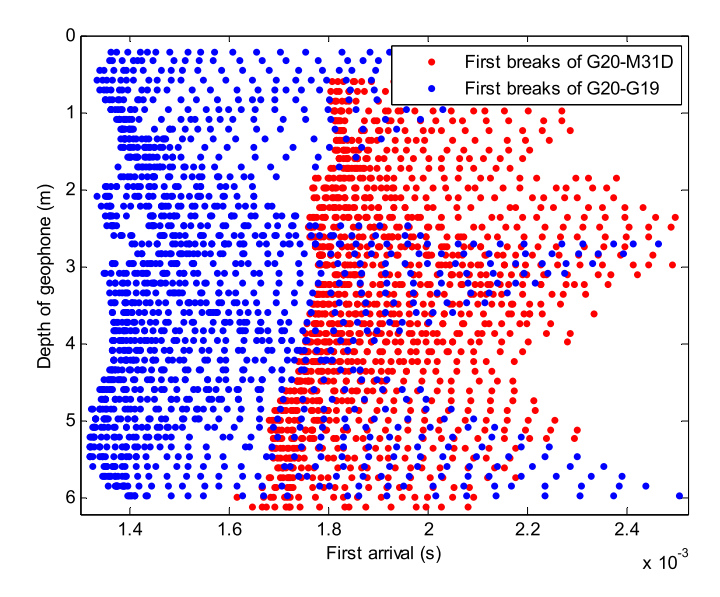


Fig. 17. Distribution of first-arrivals versus depths of geophones.

Analytical solution for the velocity model can be written as:

$$T(\mathbf{x}) = \frac{1}{|\mathbf{G_0}|} \operatorname{arccosh}\left(1 + \frac{1}{2}S(\mathbf{x})S_0|\mathbf{G_0}|^2|\mathbf{x} - \mathbf{x_0}|^2\right), \tag{16}$$

where arccosh is the inverse hyperbolic cosine function

$$arccosh(z) = ln(z + \sqrt{z^2 - 1}).$$
 (17)

Here, a 2-D example setup with the following parameters:

- $\mathbf{x_0} = (0.0, 0.0) \text{ km}$;
- Computational domain is $[0.0, 1.0] \times [0.0, 0.5]$ km;
- $S_0 = 2.0 \text{ s/km}$;
- $G_0 = \{0.0, 1.0\}$ 1/s, we set $G_0 = 1.0$ in this example.

Analytical solution and traveltimes calculated by the Podvin method, the FSM and the factored FSM are shown in Fig. 6 (a). Among which, green line stands for analytical solution, red line stands for traveltimes calculated by the factored FSM, blue line stands for traveltimes calculated by the Podvin method, and black line stands for traveltimes calculated by the FSM. Fig. 6(b) is a zoom-in map at $t=0.8\,\mathrm{s}$. Comparing with the Podvin method and the FSM, one can see that traveltimes calculated

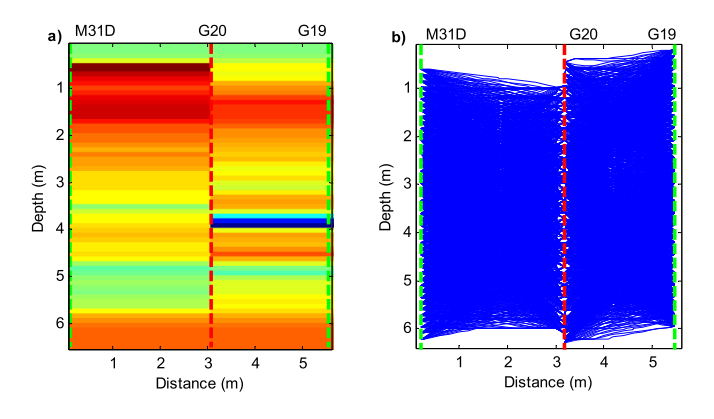


Fig. 18. Initial velocity model, and raypath distribution for M31D-G20 and G20-G19. (a) Initial velocity model built with horizontal distances and first-arrivals. (b) raypath distribution for wells M31D-G20 and wells G20-G19, after performing 20 iterations.

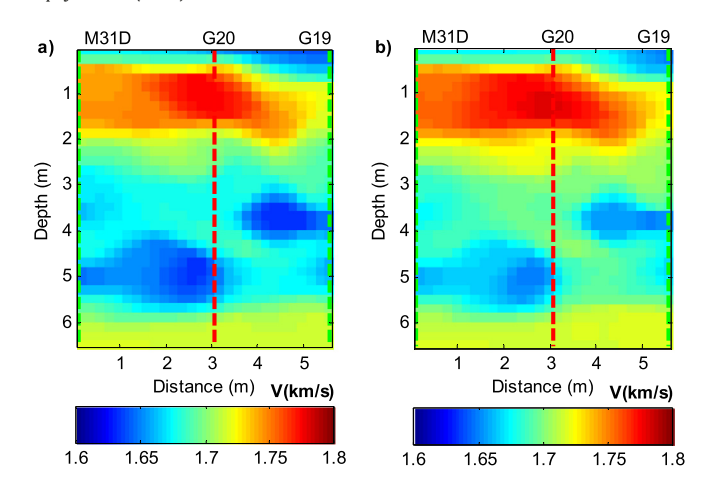


Fig. 19. Comparison of inverted velocity models. (a) velocity model obtained by the Method II, (b) velocity model obtained by the Method I.

by the factored FSM are much closer to analytical solution. In other words, the factored FSM is more accurate than the other two methods.

In order to compare traveltimes calculated with the three methods quantitatively, percentage error and traveltime difference between calculated against the analytical solution are computed. In Fig. 7, one can see that percentage error of the factored FSM is much smaller than that of the other two methods. Likewise, the traveltime difference of the factored FSM is also smaller than that of the other two methods in Fig. 8. Maximal error between analytical solution and traveltimes calculated by the Podvin method is 9.64e-3. Maximal error between analytical solution and traveltimes calculated by the FSM is 8.09e-3. However, maximal error between analytical solution and traveltimes calculated by the factored FSM is 1.26e-3. According to percentage error and traveltime difference, we can see that the factored FSM can deal with source singularity better.

4. Numerical examples

In this section, block anomaly velocity model, checkerboard velocity model, and field dataset are used for inversion. The first inversion method uses the *PStomo_eq* program directly, while the second inversion method uses the factored FSM to replace the original Podvin

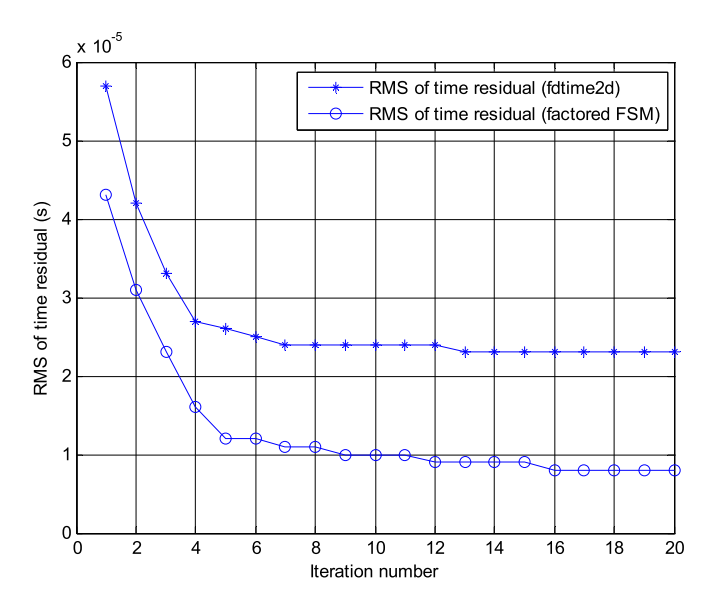


Fig. 20. Curve of RMS of traveltime residuals. (a) line with circle: convergence curve of the Method II, (b) line with asterisk: convergence curve of the Method I.

method in the *PStomo_eq* program. Here, we call the former one "Method I", and the latter one "Method II" in short.

4.1. Recovery test of velocity model with four block anomalies

In order to explore the capability of velocity inversion when it incorporates with different traveltime computation methods (the Podvin method and the factored FSM), we test them on a velocity model with four block anomalies. The only difference for traveltime calculation method is that one is the factored FSM, and the other is the Podvin method. Fig. 9(a) is the velocity model in which two anomalies with velocity 2.2 km/s, and another two anomalies with velocity 1.8 km/s. The computational domain is 204×204 m, and mesh size is 51×51 . 50 shots are distributed along top and left edges evenly, meanwhile 50 receivers are distributed along right and bottom edges evenly. Observed first-arrivals are calculated with the factored FSM on the model with mesh size 201×201 . All input parameters for the two inversions are the same. The starting model for velocity inversion is a homogeneous model with velocity 2.0 km/s, and the percentage perturbation of real against the initial model is shown in Fig. 9(b). After performing 15 iterations for two inversions, the inversion results are shown in Fig. 9(c)-(d). From which we can see the magnitude of blocks inverted by the Method II is much closer to real model than that inverted by the Method I. Fig. 10 shows the percentage perturbation of inverted against the initial model. Maximal value in Fig. 10(a) is smaller than that in Fig. 10(b). RMS of traveltime residuals is shown in Fig. 11 for the two inversions. These two inversions can both converge to a stable and small level, but the Method II can converge to a smaller level than Method I. Fig. 12 shows the percentage ratio of inverted against the real model. Percentage ratio can reach up to 78% for the Method II, while the percentage ratio is 72% for the Method I.

4.2. Recovery test of checkerboard velocity model

The two inversions are also tested on a checkerboard velocity model (Fig. 13(a)). The computational domain is 104×304 m, mesh size is 27 \times 77. Size of checker is 21 \times 20 m at depth of 0–160 m, however size of checker is 34×35 m at depth of 160-304 m. Velocity of sinusoidal anomalies is 10% perturbation of the background model (1.7 km/s). 75 shots are distributed evenly at the right well, meanwhile 75 receivers are distributed evenly at the right well. Observed first-arrivals are calculated with the factored FSM on the model with mesh size 79×229 . The background model is taken as an initial model. All input parameters are the same for the two inversions. After iterating 15 times, inverted models are shown in Fig. 13(b)-(c). From which, one can see that checkers obtained by Method II are much clearer than that inverted by Method I. Fig. 14 shows the percentage perturbation of inverted against the initial velocity model. The maximal value in Fig. 14(a) is smaller than that in Fig. 14(b). RMS of traveltime residuals is shown in Fig. 15. One can see that Method II can converge to a smaller level than Method I. The percentage ratio of inverted against the real velocity model is shown in Fig. 16. Percentage ratio for Method II can reach up to 73%, while the percentage ratio for Method I is 66%.

4.3. Field data from water contaminated site

In this example, the two inversions are used to invert a field dataset. The goal of the project is to analyze distribution of underground contaminated liquid. First arrivals of three wells (M31D, G20, and G19) are picked as observed traveltimes for velocity inversion. Well M31D, G20 and G19 locate at x = 0.2 m, x = 3.17 m and x = 5.47 m, respectively. G20 is a shot well, while M31D and G19 are receiver wells. There are 2798 source-receiver pairs in total. The computational domain is 5.6×6.4 m. Mesh size is 29×33 , so the grid spacing is 0.2×0.2 m. Curve of first-arrival versus geophone depth is shown in Fig. 17. According to inverse theory, initial model plays a significant role in

velocity inversion. Therefore, initial model is built with horizontal distance of source-receiver pairs divided by the first-arrivals. Initial velocity model is shown in Fig. 18(a). After performing 20 iterations for both inversions, raypath distribution between three wells is shown in Fig. 18 (b). From which we can see ray coverage is inferior at the top and bottom of the computational domain. Therefore, inversion result at these districts is not that reliable as in the middle district. Previous study shows that strata are mildly polluted by contamninated liquid (Ajo-Franklin et al. 2006). For the two inversions, all input parameters and initial model are the same. Fig. 19(a) is velocity model inverted by the Method II. Fig. 19(b) is velocity model inverted by the Method I. We can see two apparent low velocity areas exist at the depth of 3–6 m, but they are much clearer inverted by the Method II. Convergence curves for the two inversions are shown in Fig. 20. Similarly, Method II can converge to a smaller level than Method I.

5. Conclusions

A 2-D traveltime tomography based on the fast sweeping method for the factored eikonal equation is presented. The factored FSM can deal with source singularity problem very well when one uses finite-difference scheme solving the eikonal equation. Traveltime accuracy has been improved when it tests on a constant gradient velocity model. Eikonal solver plays a significant role in velocity inversion. Inaccurate traveltimes may distort inverted velocity model. In other words, eikonal solver has an influence on accuracy and convergence level for velocity inversion. When inversion incorporating with the factored FSM, numerical examples show that: (1) RMS of traveltime residuals can converge to a smaller level, (2) percentage perturbation of inverted against initial velocity model is smaller, (3) percentage ratio of inverted against the real velocity model can reach up to a greater value.

Acknowledgements

This research is jointly supported by the National Natural Science Foundation of China (41504095, 41664006, 41764006, 41874126), Foundation of Department of Education in Jiangxi Province (GJJ160570, 20171BCB23068), and the China Scholarship Council. Dr. Luo was partially supported by NSF DMS 1418908 and 1719907. The authors greatly appreciate Dr. Ajo-Franklin Jonathan B. in Lawrence Berkeley National Laboratory kindly provided the first arrival data, and coordinates of shots and geophones in the real data test section.

References

- Ajo-Franklin, J.B., Urban, J.A., Harris, J.M., 2006. Using resolution-constrained adaptive meshes for traveltime tomography. J. Seism. Explor. 14, 371–392.
- Aki, K., Lee, W.H.K., 1976. Determination of three-dimensional velocity anomalies under a seismic array using first P arrival times from local earthquakes, 1. A homogeneous initial model. J. Geophys. Res. 81, 4381–4399.
- Bai, C.Y., Greenhalgh, S., 2005. 3-D non-linear traveltime tomography-imaging high contrast velocity anomalies. Pure Appl. Geophys. 162, 2029–2049.
- Bai, C.Y., Tang, X.P., Zhao, R., 2009. 2-D/3-D multiply transmitted, converted and reflected arrivals in complex layered media with the modified shortest path method. Geophys. J. Int. 179, 201–214.
- Bai, C.Y., Huang, G.J., Zhao, R., 2010. 2-D/3-D irregular shortest-path ray tracing for multiple arrivals and its applications. Geophys. J. Int. 183, 1596–1612.
- Bai, C.Y., Li, X.W., Wang, D., Greenhalgh, S., 2017. The effect of ignoring Earth curvature on near-regional traveltime tomography and earthquake hypocentral determination. Pure Appl. Geophys. 174, 4329–4342.
- Benz, H.M., Chouet, B.A., Dawson, P.B., Lahr, J.C., Page, R.A., 1996. Three-dimensional P and S wave velocity structure of Redoubt Volcano, Alaska. J. Geophys. Res. 101 (B4), 8111–8128.
- Bergman, B., Tryggvason, A., Juhlin, C., 2004. High-resolution seismic traveltime tomography incorporating static corrections applied to a till-covered bedrock environment. Geophysics 69 (4), 1082–1090.
- Calvert, A.J., Fisher, M.A., 2001. Imaging the Seattle Fault Zone with high-resolution seismic tomography. Geophys. Res. Lett. 28, 2337–2340.
- Cerveny, V., 2001. Seismic Ray Theory. Cambridge University Press, Cambridge (217pp). Engdahl, E.R., Hilst, R.V.D., Buland, R., 1998. Global teleseismic earthquake relocation with improved travel times and procedures for depth determination. Bull. Seismol. Soc. Am. 88 (3), 722–743.

- Ettrich, N., Gajewski, D., 1996. Wavefront construction in smooth media for prestack depth migration. Pure Appl. Geophys. 148 (3), 481–502.
- Fischer, R., Lees J.M., 1993. Shortest path ray tracing with sparse graphs, Geophysics, 58 (7), P987–996.
- Fomel, S., Luo, S.-T., Zhao, H.-K., 2009. Fast sweeping method for the factored eikonal equation. J. Comput. Phys. 228 (17), 6440–6455.
- Hole, J., Zelt, C., 1995. 3-D finite-difference reflection traveltimes. Geophys. J. Int. 121, 427-434.
- Huang, G.-N., Zhou, B., Li, H.-X., Zhang, H., Li, Z.-L., 2014. 2D seismic reflection tomography in strongly anisotropic media. J. Geophys. Eng. 11, 1–8.
- Huang, G.-N., Zhou, B., Li, H.-X., Nobes, D.-C., 2017. Seismic traveltime inversion based on tomographic equation without integral terms. Comput. Geosci. 104, 29–34.
- Kennett, B.L.N., Engdahl, E.R., Buland, R., 1995. Constraints on seismic velocities in the Earth from traveltimes. Geophys. J. Int. 122, 108–124.
- Kim, S., Cook, R., 1999. 3-D Traveltime Computation using Second-Order ENO Scheme. Geophysics 64, 1867–1876.
- Lambare, G., Lucio, P.S., Hanyga, A., 1996. Two-dimensional multivalued traveltime and amplitude maps by uniform sampling of a ray field. Geophys. J. Int. 125, 584–598.
- Lees, J.M., 1992. The magma system of Mount St. Helens non-linear high-resolution P-wave tomography. J. Volcanol. Geotherm. Res. 53, 103–116.
- Leidenfrost, A., Ettrich, N., Gajewski, D., Kosloff, D., 1999. Comparison of six different methods for calculating traveltimes. Geophys. Prospect. 47, 269–297.
- Lions, P.L., 1982. Generalized Solutions of Hamilton-Jacobi Equations. Pitman Advanced Publishing Program.
- Luo, S.-T., Qian, J.-L., 2012. Factored singularities and high-order Lax-Friedrichs sweeping schemes for point-source traveltimes and amplitudes. J. Comput. Phys. 230, 4747–4755
- Marti, D., Carbonell, R., Flecha, I., 2008. High-resolution seismic characterization in an urban area Subway tunnel construction in Barcelona, Spain. Geophysics 73 (2), PM1, PEO.
- Moser, T.J., 1991. Shortest path calculation of seismic rays, Geophysics, 56(1), P59-67.
- Nakanishi, I., Yamaguchi, K., 1986. A numerical experiment of nonlinear image reconstruction from first-arrival times for two-dimensional island arc structure. J. Phys. Earth 34, 195–201.
- Podvin, P., Lecomte, I., 1991. Finite difference computation of traveltimes in very contrasted velocity models a massively parallel approach and its associated tools. Geophys. J. Int. 105, 271–284.
- Qian, J., Symes, W., 2002. An adaptive finite-difference method for traveltimes and amplitudes. Geophysics 76 (1), 167–176.
- Qin, F.-H., Luo, Y., Olsen, K.B., Cai, W.Y., Schuster, G.T., 1992. Finite-difference solution of the eikonal equation along expanding wavefronts. Geophysics 57 (3), 478–487.

- Rawlinson, N., Fishwick, S., 2012. Seismic structure of the southeast Australian lithosphere from surface and body wave tomography. Tectonophysics 572, 111–122.
- Sethian, J., Popovici, M., 1999. 3-D traveltime computation using the fast-marching method. Geophysics 64 (2), 516–523.
- Tryggvason, A., Bergman, B., 2006. A traveltime reciprocity discrepancy in the Podvin and Lecomte time3d finite difference algorithm. Geophys. J. Int. 165, 432–435.
- Tryggvason, A., Rognvaldsson, S.T., Flovenz, O.G., 2002. Three-dimensional imaging of the P- and S-wave velocity structure and earthquake locations beneath Southwest Iceland. Geophys. I. Int. 151, 848–866.
- Tryggvason, A., Schmelzbach, C., Juhlin, C., 2009. Traveltime tomographic inversion with simultaneous static corrections—well worth the effort. Geophysics 74 (6), WCB25—WCB33
- Tsai, Y.-H., Cheng, L.-T., Osher, S., Zhao, H.-K., 2003. Fast sweeping algorithms for a class of Hamilton-Jacobi equations. SIAM J. Numer. Anal. 41 (2), 673–694.
- Van, T.J., Symes, W.W., 1991. Upwind finite-difference calculation of traveltimes. Geophysics 56 (6), 812–821.
- Vesnaver, A.L., Accaino, F., Bohm, G., Moro, G.D., 2003. Time-lapse tomography. Geophysics 68 (3), 815–823.
- Vidale, J., 1988. Finite-difference calculation of travel times. Bull. Seismol. Soc. Am. 78 (6), 2062–2076
- Vidale, J., 1990. Finite-difference of calculation of traveltimes in three dimensions. Geo-
- physics 55 (5), 521–526. Vinje, V., Iversen, E., Gjoystdal, H., 1993. Traveltime and amplitude estimation using
- wavefront construction. Geophysics 58, 1157–1166.
 Vinje, V., Astebol, K., Iversen, E., Gjoystdal, H., 1999. 3-D ray modeling by wavefront construction in open models. Geophys. Prospect. 64, 1912–1919.
- Wang, Y.H., 2014. Seismic ray tracing in anisotropic media: a modified Newton algorithm for solving highly nonlinear systems. Geophysics 79, T1–T7.
- Yordkayhun, S., Tryggvason, A., Norden, B., Juhlin, C., Bergman, B., 2009. 3D seismic traveltime tomography imaging of the shallow subsurface at the CO2SINK project site, Ketzin, Germany. Geophysics 74 (1), G1–G15.
- Zelt, C.A., Azaria, A., Levander, A., 2006. 3D seismic refraction traveltime tomography at a groundwater contamination site. Geophysics 71, H67–H78.
- Zhao, H.-K., 2004. A fast sweeping method for eikonal equations. Math. Comput. 74 (250), 603–627.
- Zhou, H.-W., 2006. First-break vertical seismic profiling tomography for Vinton Salt Dome. Geophysics 71 (3), U29–U36.
- Zhou, B., Greenhalgh, S.A., 2006. Ray path and travel time computations for 2D transversely isotropic media with dipping symmetry axes. Explor. Geophys. 37 (2), 150–159.